Obtaining tertiary protein structures by the ab-initio interpretation of small angle X-ray scattering data

Christopher Prior,[*,†] Owen R Davies,[‡] Daniel Bruce,[¶,§] and Ehmke Pohl[*,¶,§]

†*Department of Mathematical Sciences, Durham University, Durham DH1 3LE, United Kingdom*

‡*Institute for Cell and Molecular Bioscience, Medical School, University of Newcastle, Newcastle upon Tyne, NE2 4HH,United Kingdom*

¶*Department of Biosciences Durham University, Durham DH1 3LE, United Kingdom*

§*Department of Chemistry, Durham University, Durham DH1 3LE, United Kingdom*

E-mail: christopher.prior@durham.ac.uk; ehmke.pohl@durham.ac.uk

Abstract

Small angle X-ray scattering (SAXS) is an important tool for investigating the structure of proteins in solution. We present a novel ab-initio method representing polypeptide chains as discrete curves used to derive a meaningful three-dimensional model from **only** the primary sequence and SAXS data. High resolution structures were used to generate probability density functions for each common secondary structural element found in proteins, which are used to place realistic restraints on the model curve's geometry. This is coupled with a novel explicit hydration shell model in order derive physically meaningful 3D models by optimizing against experimental SAXS data. The efficacy of this model is verified on an established benchmark protein set, then it is used to predict the Lysozyme structure using only its primary sequence and SAXS

data. The method is used to generate a biologically plausible model of the coiled-coil component of the human synaptonemal complex central element protein.

Introduction

Biological small angle X-ray scattering (BioSAXS) is an increasingly important method for characterising protein structures in solution.[1–3] Its primary advantages over complmentary techniques such as crystallography and NMR is its ability to provide information under native conditions about large protein molecules not accessible by complementary methods. However, there is a price to pay for this advantage; the random motion and orientation of molecules in solution leads to a loss of information due to an effective averaging of the scattering, leaving only information about the protein's intra-molecular distances not their spatial orientations.[4] The correct interpretation leading to meaningful biological results remains therefore challenging.[5]

Two main methods have been developed to interpret BioSAXS data. The first assumes an accurate 3D model of the protein backbone, usually derived from X-ray crystallography.[6–9] This model is used to calculate the X-ray scattering curve once the excluded solvent volume is taken into account. A major advance, first presented in the CRYSOL algorithm,[6] was the inclusion of the solvation layer - the ordered water molecules at the surface of the protein. CRYSOL as well as the FOXS package, developed by Schneidmann-Duhovny *et al*,[7] adjust an implicit "shell" of scattering (implicit meaning they do not model individual solvent molecules). Other packages treat the shell explicitly using either molecular dynamics (AquaSAXS)[8] or a geometric filling approach (the SCT suite).[9] Allowing for a shell which can have gaps and fill cavities in the protein model gives a more reliable fit to the data.[5] An extension of this approach is to use all atomistic modeling with PDB structures as a start point,[10,11] the application of such techniques, however, can require significant technical expertise. The second method does not assume an initial structure (ab-initio) but simplifies

the protein model as either a volume[12] or a chain[13] of scattering beads without explicit secondary structure. These methods are hence applicable to *de novo* structural prediction, but the lack of secondary structure means interpreting these predictions is a difficult task.[5]

Here we propose an alternative ab-initio technique which uses a curve model of the 3D structure of the polypeptide chain, this description has a much reduced number of parameters by comparison to all atomistic models. Similar curve models have been previously proposed[14–16] but not for the purpose of interpreting BioSAXS data. The model is parameterised by consecutive discretised descriptions of the four major secondary structural elements, α-helices, β-strands, flexible sections and random coils. The permissible geometry of these curves is restricted by empirically determined constraints, which are akin to Ramachandran constraints.[17] To use the model for interpretation of BioSAXS data the polypeptide chain model is combined with a water model for the first hydration shell and an empirically calibrated scattering model. The geometry of the model can then be optimized against the experimental BioSAXS data. A critical factor, novel to our curve representation of the polypeptide chain, is the construction of empirical probability distributions for the model parameters. These distributions serve the dual purpose of preferencing commonly observed secondary structures in the set of potential chain models, whilst simultaneously allowing for predictions with rare/novel but physically permissible secondary structure. An advantage of this mthod for ab-initio interpretation of BioSAXS data, by comparison to the established bead models,[12,13] is that by accurately characterizing the protein's secondary structure it can reliably incorporate additional structural information in order to improve the results of the technique. In this study contact predictions, based on sequence alignments alone, are used to improve the model predictions. A final advantage of the code developed is that its only input requirements are the primary sequence and scattering data, so places only basic technical requirements on the user for its use.

We first applied this new methodology to data of well characterized model protein Lysozyme before moving to the BioSAXS data of structural core of the human synaptonemal

complex central element protein 1 (SYCE1). This protein represents an essential structural component of the synaptonemal complex (SC) that binds together homologous chromosomes during meiosis and provides the necessary three-dimensional environment for crossover formation.[18–20] The SC is formed of oligomeric α-helical coiled-coil proteins that undergo self-assembly to create a lattice-like assembly.[21–23] In a recent biochemical and biophysical study, human SYCE1 was shown to adopt a homodimeric structure in which its structural core is provided by residues 25-179 forming an anti-parallel coiled-coil.[24] Further, the structural core was expressed in an engineered construct in which two SYCE1 25-179 sequences were tethered together through a short linker sequence (GQTNPG). This construct faithfully reproduced the native structure, and substantially improved protein stability in solution.[24] In this study, using secondary structure predictions and distance restraints purely based on the sequence of the protein alone, an excellent model of an anti-parallel extended but bent coiled-coil is derived, which is fully consistent with biological data.

Methods

First we describe the reduced parameter protein model we use to interpret the BioSAXS data. This is composed of a polypetide chain curve model with a surrounding explict hydration shell. Empirically calibrated structure factor functions for each constituent element of the model are constructed to produce theoretical scattering curves for this tertiary structure model.

Polypeptide chain

The polypeptide chain is represented as a set of points in 3D space $\{\mathbf{c}_i\}_{i=1}^{n}$, the positions of the C^{α} atoms in each amino acid. The geometry of four consecutive points $(\mathbf{c}_i, \mathbf{c}_{i+1}, \mathbf{c}_{i+2}, \mathbf{c}_{i+3})$ can be characterized by two parameters, the curvature κ and torsion τ. κ is defined by the unique sphere made by the centre of the joining edges (see Figure 1(a)), the smaller the

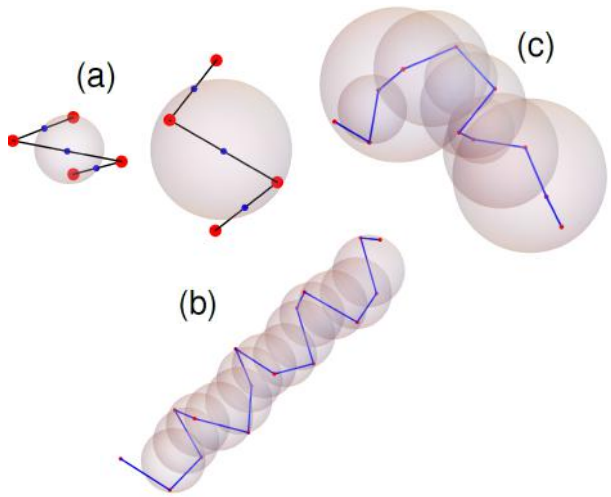

Figure 1: Figures depicting elements of the backbone model. (a) curve subsections $(\mathbf{c}_i, \mathbf{c}_{i+1}, \mathbf{c}_{i+2}, \mathbf{c}_{i+3})$ (red points) and their mid section points $(\mathbf{c}_{m1}, \mathbf{c}_{m2}, \mathbf{c}_{m3})$ (blue), the first example is more tightly wound and has a smaller sphere, hence a higher κ value. The sphere defined by these mid-section points is shown, the inverse of it's radius is the curvature κ. (b) an α-helical section with uniformly similar (κ, τ) values. (c) a flexible (linker) section with varying (κ, τ) values.

sphere the more tightly the curve joining the points fold on themselves, τ measures the chirality of the section, it is positive for right-handed coiling negative if left-handed. More precise definitions are as follows:

Curvature κ

A section of four residues defined by the points $(\mathbf{c}_i, \mathbf{c}_{i+1}, \mathbf{c}_{i+2}, \mathbf{c}_{i+3})$ defines three edges with midpoints $\mathbf{c}_{ml} = (\mathbf{c}_{i+l-1} + \mathbf{c}_{i+l})/2$, which in turn define the curvature sphere.[1–3] The curvature, the inverse of its radius is

$$\kappa(\mathbf{c}_{m1}, \mathbf{c}_{m2}, \mathbf{c}_{m3}) = \frac{2|\sin(\theta_{123})|}{||\mathbf{c}_{m1} - \mathbf{c}_{m2}||} \tag{1}$$

where θ_{123} is the angle between the vectors $\mathbf{c}_{m1} - \mathbf{c}_{m3}$ and $\mathbf{c}_{m2} - \mathbf{c}_{m3}$.

Torsion τ

Three points define a plane (with unit normal vector $\mathbf{n}$) and the four points $(\mathbf{c}_i, \mathbf{c}_{i+1}, \mathbf{c}_{i+2}, \mathbf{c}_{i+3})$ define two planes through their unit normal vectors $\mathbf{n}_2$ and $\mathbf{n}_2$ respectively:

$$\begin{aligned} \mathbf{n}_\alpha &= \mathbf{N}_\alpha/||\mathbf{N}_\alpha||,\ \alpha = 1, 2, \\ \mathbf{N}_1 &= (\mathbf{c}_{i+1} - \mathbf{c}_i)\times(\,\mathbf{c}_{i+2} - \mathbf{c}_{i+1}), \\ \mathbf{N}_2 &= (\mathbf{c}_{i+2} - \mathbf{c}_{i+1})\times(\,\mathbf{c}_{i+3} - \mathbf{c}_{i+2}). \end{aligned} \tag{2}$$

The torsion is the (length weighted) angle these planes make with each other,

$$\begin{aligned} \tau(\mathbf{c}_i, \mathbf{c}_{i+1}, \mathbf{c}_{i+2}, \mathbf{c}_{i+3}) &= \frac{2}{l}\sin(\theta_n/2), \\ l &= (||\mathbf{c}_{i+1} - \mathbf{c}_i|| + ||\mathbf{c}_{i+2} - \mathbf{c}_{i+1}|| + ||\mathbf{c}_{i+3} - \mathbf{c}_{i+2}||)/3. \end{aligned} \tag{3}$$

with θ_n is the angle between $\mathbf{n}_1$ and $\mathbf{n}_2$, see *e.g.*[25]

The algorithm for generating a curve of length n from $n-3$ pairs of values of (κ_i, τ_i) is as follows: Consider a section of curve of length m and $m-3$ pairs (κ_i, τ_i), whose three initial points $\mathbf{c}_1, \mathbf{c}_2, \mathbf{c}_3$ are randomly chosen (with fixed separation distance $R = 3.8$). Since scattering expressions are invariant under an arbitrary translation and rotation ([4]) the exact values of the first two points do not matter (as long as their separation is R). The third point is a structural degree of freedom but it is restricted such that the C^α-C^α distance between $\mathbf{c}_1$ and $\mathbf{c}_3$ is greater than R. Once these points are specified the fourth point will be

$$\mathbf{c}_4 = \mathbf{c}_3 + R\left(\sin(\theta)\cos(\phi), \sin(\theta)\sin(\phi), \cos(\theta)\right). \tag{4}$$

with $\theta = \in [0, \pi], \phi \in [0, 2\pi]$. The set $(\mathbf{c}_1, \mathbf{c}_2, \mathbf{c}_3, \theta, \phi)$ define four points and hence κ and τ values. Using values of κ_1 and τ_1 equations (1) and (3) are solved for θ and ϕ, this gives $\mathbf{c}_4$. The next point $\mathbf{c}_5$ can similarly be found from the values κ_2 and τ_3, and so on until all

$m-3$ (κ_i, τ_i) have been used to yield the m points $\mathbf{c}_i$. Examples of an alpha-helical and flexible linker sections (taken from the structure of Bovine serum albumin (PDB=3V03)[26]) are shown in Figure 1(b) and (c).

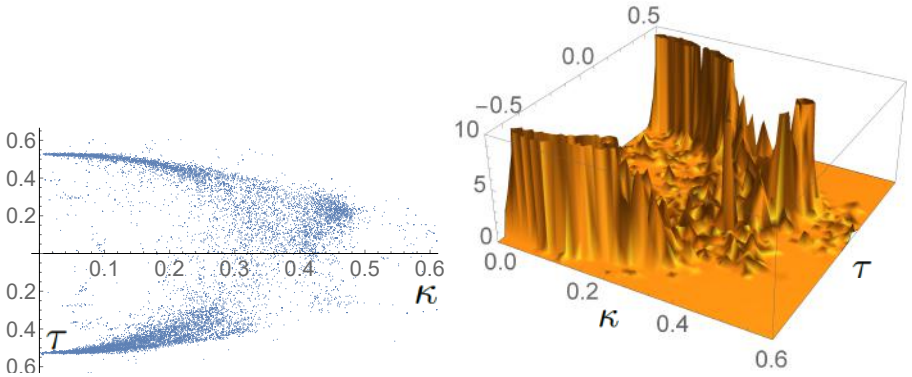

(a) (b)

Figure 2: Illustrations of the κ-τ spaces used to impose realistic geometry constraints on the polypeptide chain. (a) (κ, τ) pairs obtained from crystal structures, plotted as points with κ on the horizontal axis and τ the vertical axis. (b) is a P.D.F, created from the data in (a), which correspond to linker sections. There are three distinct domains of high probability corresponding to the preferred corresponding to the preferred secondary structural elements.

Secondary structure geometry restraints

In order to derive geometric constraints C^{α} coordinates were extracted from over from a set of over 60 protein structures for which high-resolution crystal structures are available in the Protein Data Base (PDB) and the κ and τ values calculated for all sub-sections $(\mathbf{c}_i, \mathbf{c}_{i+1}, \mathbf{c}_{i+2}, \mathbf{c}_{i+3})$. The κ-τ pairs are shown in Figure 2(a). There are three main populations of values (preferential regions). As shown in section 1.3 of the supplementary material these regions of (κ, τ) space correspond to the three preferential domains of Ramachandran space.[17] Using the PDB's secondary structure annotation this data was split into categories of β-strands, α-helices and the rest which are not identified (referred to here as linkers). To account for random coils the data were further divided into subsets whose values remained in one preferential domain (as in Figure 1(b)) and those whose κ-τ values belong to multiple domains (like Figure 1(c)). For each set of data a representative probability density function

(P.D.F.) was calculated using Kernel smoothing techniques[27] (for details see sections 1.4 and 1.5 of the supplementary material), an example is shown in Figure 2(b).

Generating models from secondary structure annotation

In order to generate models based on secondary structure information alone a protein of n amino acids is split into l distinct sub-domains of length m_i ($\sum_{i=1}^{l} m_i = n$). Each section l is classified as α-helical, β-strand or linker, for the purpose of testing and calibration the PDB file's secondary structure assignment was used to perform this task. For each section of length m_i, $m_i - 3$ (κ, τ) pairs are drawn from an appropriate P.D.F. and the section is constructed. This process creates the l individual secondary structures, which must then be linked together. Two neighboring sections with specified geometry (for example an α helix and linker) still have a relative rotational degree of freedom. To ensure this remains physically realistic the geometry of the last three and first C^{α} positions of neighboring secondary sections were extracted from the PDB set and further PDF's for the set of permissible (κ, τ) pairs of these joining sections were generated for each type of join (*i.e.* α-helix to linker or linker to β strand). So the final step of the process is to obtain all (κ, τ) values for the joint geometry and then construct the whole backbone. A precise mathematical description of this algorithm, *constrained backbone algorithm* (**CB**), is given in section 1.6 of the supplement. One example of a structure generated using this algorithm is shown in Figure 6(b), this particular structure was used as a starting point for an ab-initio structure optimization in this study.

The hydration layer

Once the curve representation is obtained it is crucial to include a model of the hydration layer in order to generate realistic scattering curves. To this aim solvent molecules are placed in-between a pair of cylindrical surfaces surrounding the axis of a section of the backbone (Figure 3(a)). This layer is then reduced by removing all overlapping solvent molecules. This ensures the shell remains in hollow sections between the fold and on the protein surface, whilst

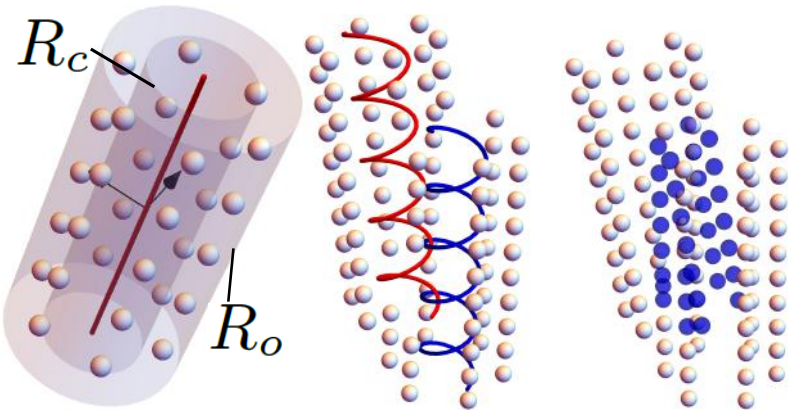

Figure 3: Visualizations of the hydration layer model. (a) the initial solvent layer, shown as silver spheres with the core R_c and outer R_o cylinders surrounding the axis of the section (red curve). (b) overlapping sections and solvent layers, (c) shows, in blue, the removed solvent molecules of the pair of sections shown in (b).

the water molecules are removed form significantly folded regions. This is a crucial aspect of our hydration layer model as it has been shown that one **needs** to allow for inhomogenous hydration layers in order to avoid inaccurate predictions from BioSaxs data.[28] This method is illustrated in Figure 3 where the two cylinders of radius R_c (core) and R_o (outer), $R_o > R_c$ are centered on a section i's helical axis (a). Consider a solvent molecule belonging to another section j whose nearest distance from the axis of section i is R_s. If $R_s < R_c$ the solvent is too close to the backbone and removed. If $R_c < R_s < R_o$ the solvent is classed as being shared by the sections i and j and only counted once.

This process is applied to all solvent molecules from section i and j on each other, an example of the outcome is shown in Figures 3(b) and (c). Applying this process pairwise to all sections of a C^{α} backbone yields the final hydration layer.

The exact mathematical description of this hydration layer is detailed in sections 2.1-2.3 of the supplement. The values of the radii (R_c, R_o) and a number of other parameters controlling the solvent density were determined by fitting the model to high resolution crystal structures which contained the first hydration shell. An example model shell, generated with these parameters, is shown in comparison to the model solvent positions from the subatomic

resolution structure of a phosphate binding protein from the PDB 4F1V[29] in Figure 4. It is shown the two distributions are statistically similar in section 2.4 of the supplement and hence that the model is a realistic representation of the average positions of the inner hydration shell.

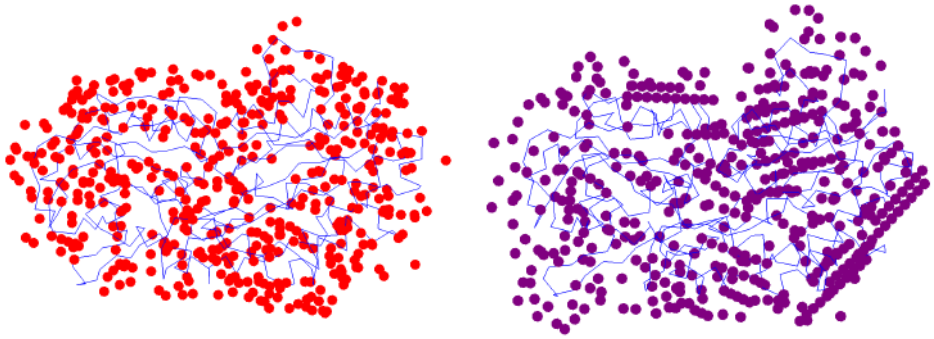

(a) (b)

Figure 4: Comparisons of crystallographic and model solvent positions from the crystal structure of a phosphate binding protein PDB=4F1V, determined at an ultra- high resolution of 0.88 Å .[29] (a) the PDB backbone and the relevant solvent molecules. (b) the model solvent positions (surrounding the same curve as in (a)) obtained with the experimentally determined hydration shell model parameters.

The scattering formula

Once the polypeptide chain and hydration layer models are determined, the Debye formula,[30]

$$I(q) = \sum_{i=1}^{N} \sum_{j=1}^{N} f_i(q) f_j(q) \frac{\sin(q r_{ij})}{q r_{ij}}, \tag{5}$$

is used to calculate the scattered intensity $I(q)$ as a function of momentum transfer $q = \pi \sin(\theta)/\lambda$. Here N is total number of C^{α} 's and solvent molecules and $f_i(q)$ the form factor for residue i. There are two types, one for an amino acid with an excluded volume correction and one for a solvent molecule which are defined as follows:

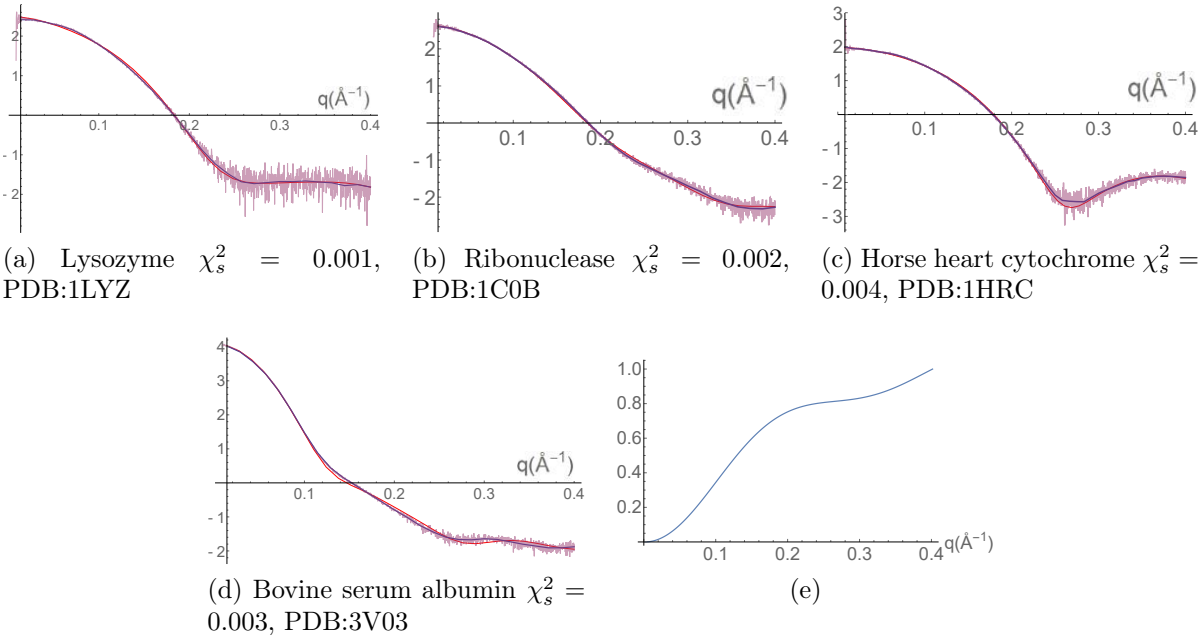

(a) Lysozyme $\chi_s^2 = 0.001$, PDB:1LYZ

(b) Ribonuclease $\chi_s^2 = 0.002$, PDB:1C0B

(c) Horse heart cytochrome $\chi_s^2 = 0.004$, PDB:1HRC

(d) Bovine serum albumin $\chi_s^2 = 0.003$, PDB:3V03

(e)

Figure 5: Fits to scattering data for various molecules using appropriate C^α coordinates as a backbone model $\{\mathbf{c}\}_{i=1}^n$ (see chapter 3 of the supplementary notes for details). In panels (a)-(d) The data scattering data is shown overlayed by the smoothed data used for fitting (blue curve) and and the model fit (red curve). Panel is the (e) the averaged scattering function f_{am}^{ex} obtained by averaging the scattering parameters obtained from fits like those shown in (a)-(d).

Amino acid form factors

The form factor f_{am} of an amino acid, centered on the C^α atom position, are

$$f_{am}(q) = f_b(q) - \rho_{ex} f_{ex}(q), \tag{6}$$

where f_b is the scattering of the amino acid in a vacuum, f_{ex} is the adjustment due to the excluded volume of solvent and ρ_{ex} a constant. Each amino acid is assigned the same scattering function $f_b(q)$, a five-factor exponential representation

$$f_b = \sum_{i=1}^{5} A_i \mathrm{e}^{-B_i q^2} + C, \tag{7}$$

where $\{A_i, B_i\}_{i=1}^{5}$ and C are empirically determined constants (a standard form used to fit molecular form factors[31]). The excluded volume effect is captured using an exponential model in the form

$$f_{ex}^{a}(r_w, q) = v(r_w)\mathrm{e}^{-\pi q^2 v(r_w)^{3/2}}, \quad v(r_w) = \frac{4\pi}{3} r_w^3, \tag{8}$$

where r_w is the average atomic radius of the atom.[6,7,13] To calculate the excluded volume for amino acids coordinates for all 20 amino acids,[32] and values of r_w for Carbon, Nitrogen, Oxygen, Hydrogen and Sulphur (*e.g.*[33]) were used to compute the excluded volume scattering, centered at the C^{α}, through

$$f_{ex}^{am}(q) = \sum_{i=1}^{N_{am}} f_{ex}^{a}(r_{wi}, q) \frac{\sin(q r_i^{\alpha})}{q r_i^{\alpha}}, \tag{9}$$

where r_i^{α} is the distance of atom i from the C^{α} molecule and N_{am} the number of atoms in the amino acid. Since f_b does not discriminate individual amino acids this value f_{ex}^{am} was averaged over all 20 amino acids, weighted by their abundance in globular proteins (see[34]). This averaged function, shown in Figure 5(e), gives $f_{ex}(q)$. Finally (6) includes a constant ρ_{ex} which modulates the effect of the excluded volume scatter by comparison to f_b, this value is constrained to lie within 0.75 and 1.25 (similar constraints are used in[6,7,13]). The scattering form for an individual water molecule in the hydration layer is

$$f_h(q) = \rho_h(2f_{hy}(q) + f_{ox}(q)), \tag{10}$$

where f_{hy} and f_{ox} are the vacuum scattering of Hydrogen and Oxygen respectively.[31] The constant ρ_h was empirically determined (as in[7]). A detailed description of the parameter determination method is given in Section 3 of the supplementary notes.

Evaluating structural similarity.

In the next step the geometry of each model generated by the CB algorithm is optimized by refinement against the scattering data. However, since the problem is under-determined, many models will fit the experimental data so a method is required to compare structures and determine which predictions are "essentially the same" in that they only differ by small local conformational changes (as one should expect in solution). The standard methods in protein crystallography for comparing similar protein structures are based on root mean squared deviations (RMSD) where two structures are superimposed to minimize the sum of all distances of equivalent paired atoms.[35,36] This measure and variants on it are known to be overly sensitive to large deviations in single loops (as discussed in[35]). Unlike homologous crystal structures, which will often only differ by the change in a small subsection of the whole structure, the comparison here will be made between structures generated by a random algorithm, so the significant build up of relatively small individual RMSD errors is likely. In section 2.1 of the supplement a number of additional problems with using the RMSD measure in this context are discussed in detail. To mitigate these problems a novel and more robust approach based on knot theoretic techniques was developed.

Knot fingerprints

Techniques from knot theory have previously been applied to identify specific (knotted) entanglements in protein structures.[37] To compare two protein structures using knot theory the N and C termini need to be joined.[38] As in[37] the procedure used here is to surround the backbone with a sphere, then choose two random points on the sphere and join the end termini to these points, finally this extended curve is closed with a geodesic arc. The knot is then classified (*e.g.* via Jones polynomials). This procedure is repeated a significant number of times (10000 in this study) and the most common knot (MCK) chosen to indicate the knotting of the curve. To obtain additional information the MCK is calculated for all subsets $\{\mathbf{c}_i |\, i = k, k+1 \ldots j,\, j > k,\, j - k > 3\}$ of the curve. One can then plot this data on

a “staircase" diagram with j and k on the axes and each square of the domain colored by its most common knot (*e.g.*[39]) (examples of staircase diagrams are shown in Figure 6(c), (d) and (e)). The fingerprint is found to be preserved across protein families,[39] even when there is low sequence identity.[40]

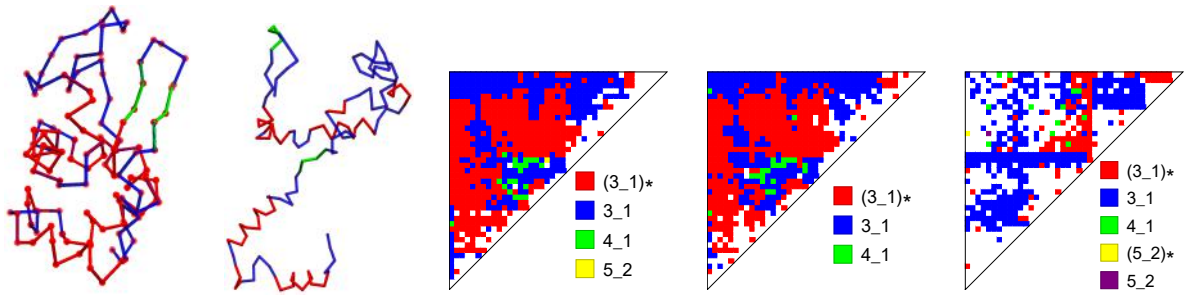

(a) (b) (c) (d) (e)

Figure 6: Secondary knot fingerprint analysis of the Lysozyme structure. (a) The C^{α} trace of Lysozyme (PDB 1LYZ[41]). The α-helices are shown in red, β-strand structures green, and linker sections light blue. (b) A random structure generated using the CB algorithm which has the same secondary structural elements as Lysozyme. This could be a starting model for the fitting procedure. Panels (c) and (d) are secondary fingerprints of two different crystal structure of Lysozome (1LYZ and the 1AKI respectively). The knot types are indicated (Rolfsen classification[42]), white spaces indicate no secondary knots (all knots were of the primary type). (e) Secondary fingerprint for the random structure shown in (b), it differs significantly from (c) and (d) and has a larger range of knots present.

Secondary knot fingerprints

Figure 6(c) is the knot fingerprint for one set of Lysozyme coordinates (shown in Figure 6(a)), of the **second** most common knot identified during the random closure process. The secondary fingerprint shown in 6(d) is from a second set of Lysozyme coordinates, (c) and (d) are significantly similar. The secondary fingerprint (e) is derived from a CB generated backbone model, shown in (b), which has the same secondary structure sequence as the 1LYZ PDB. The secondary fingerprint differences between the correct structure (c) and the randomly generated structure (d) is immediately obvious. All primary (MCK) fingerprints in these cases are *identical* and all have the unknot as the MCK. It is clear secondary (and possibly tertiary) knot fingerprints can differentiate un-knotted folds. A knot fingerprint

statistic $\mathcal{K}_l(K_1, K_2)$ is defined in section 4.2 of the supplement which quantifies the weighted similarity of knot fingerprints at level l associated with the curves K_1 and K_2 ($l = 2$ for Figures 6(c)-(e)); it yields a value between 0, completely dissimilar, and 1, identically folded.

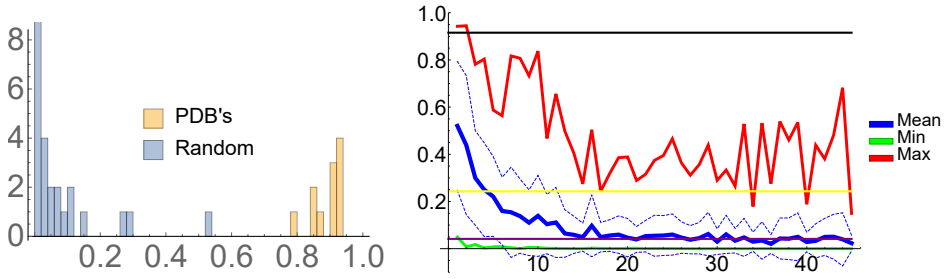

(a) (b)

Figure 7: Properties of the (secondary) knot fingerprint statistic $\mathcal{K}_2$ based on variations of the Lysozyme structure. (a) Secondary knot statistics $\mathcal{K}_2(K_{1LYZ}, K)$ of various structures K compared to the curve shown in Figure 6(a). The two distinct sets are Lysozyme PDB's and random structures with secondary structure alignment to Lysozyme (generated using the CB algorithm). (b) Plots of the mean, maximum and minimum value of the 50 secondary knot statistics comparing the 1LYZ structure and the same structure subjected to n random changes in its secondary structure. The dotted lines show 1 standard deviation from the mean. The black line is the average of the PDB structure secondary fingerprint statistics (see (a)) the purple line the Random structure average (crossing the mean at about $n = 15$) and the yellow line the average of secondary fingerprint values for models which fit the experimental data (crossing the mean at about $n = 3$).

In section 4.3 of the supplement it is demonstrated that the statistic has the following properties. Firstly it quantifies crystal structures of the same molecule as highly similar $\mathcal{K}_2(K_1, K_2) > 0.77$ and randomly generated structures (with the same secondary structure sequence) as significantly dissimilar, generally $\mathcal{K}_2(K_1, K_2) < 0.1$ (see Figure 7(a)). Secondly it judges crystal monomer structures of similar length as being significantly different (typically $\mathcal{K}_2 < 0.4$), *i.e.* it can differentiate folds. Thirdly it is shown to have excellent properties under deformation. To demonstrate, n randomly distributed changes were applied to a crystal structure K_{pdb} using the CB algorithm. For each n 50 such structures K_n were generated and the values of the statistic $\mathcal{K}_2(K_{pdb}, K_n)$ calculated. The results are plotted as a function of n in Figure 7(b) for Lysozyme. The mean value drops off rapidly to the same value as the average of the randomly generated structures (after about 15 changes). The maximum

value always remains significantly higher than the mean, it drops below PDB quality after only 2 changes. So a high $\mathcal{K}_2(K_{pdb}, K_n)$ value > 0.75 indicates the structure is likely largely the same as the original structure.

Experimental data fitting

The following chi -square statistic χ_f^2 is used to to asses the fit quality of a model predictions

$$\chi_f^2 = \frac{1}{n_s - 1} \sum_{i=1}^{n_s} \left[\log(I_m(q_i)) - \log(I_e^s(q_i)) - L_d\right]^2, \tag{11}$$
$$L_d = \frac{1}{n_s} \sum_{i=1}^{n_s} \log(I_m(q_i)) - \log(I_e^s(q_i)).$$

Where n_s is the discrete number of points on the domain $q \in [0, 0.4]$ on which the scattering is sampled (a commonly used domain *e.g.*[7]). I_m is the model scattering calculated using the Debye formula (5) and I_e^s, the smoothed experimental data (smoothed using the procedure described in[43] which is designed to avoid over-fitting). The factor L_d, which will superimpose identical curves which differ by a translation, is used because the protein concentration can only be measured with relatively low accuracy[6,7] (when taking a logarithm of the data a scaling factor becomes a vertical translation). In addition, to prevent chemically unreasonable conformations, a penalty is applied if the C^α-C^α distance of ≤ 3.8 occurs for any pair of non-adjacent C^α positions, this quantity is labelled χ_{nl}. The initial model is optimized as described above until $\chi_f^2 + \chi_{nl} < 0.008$. Values below this threshold represent an excellent fit to the scattering data, as shown in Figure 8(d). This value is based on a comparison to other studies (see Section 3.6 of the supplement).

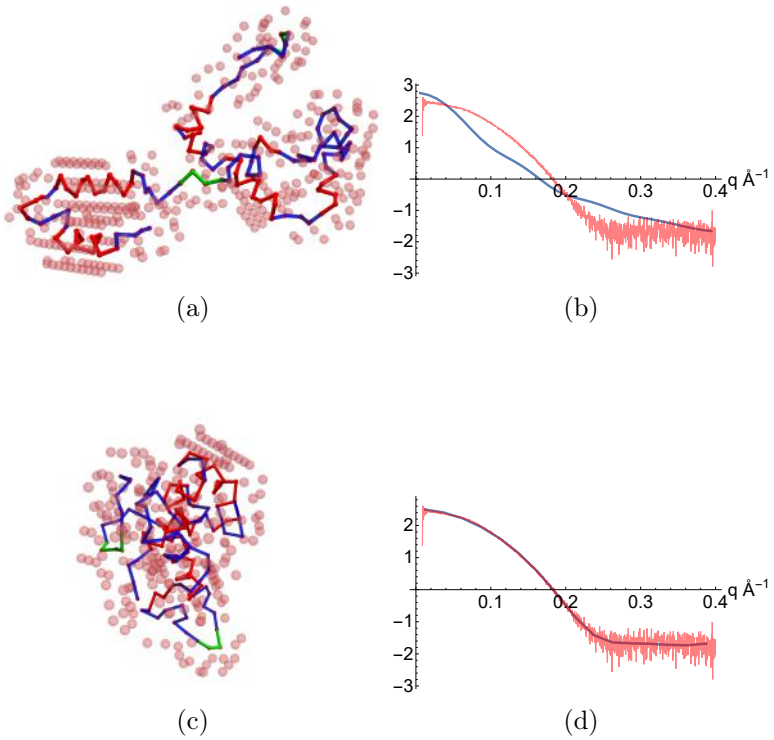

Figure 8: Figures illustrating the fitting process. (a) An initial configuration of the backbone based only on the secondary structure assignment of Lysozyme (PDB:1LYZ). Also shown as spheres are the molecules of the hydration layer. (b) The model scattering curve compared the BioSAXS data. (c) a final structure (and hydration layer) obtained from the fitting process and its model scattering curve now fitting the BioSAXS data well (d).

Results

Validation of the backbone curve and water model

As discussed in the methods section, each part of the model, the C^{α} backbone, the explicit hydration layer and the scattering model have individually been designed and verified using actual structures from the protein data bank. However, it remains to demonstrate the composite model's efficacy. To test this it was applied to the benchmark set of proteins used to compare the set of atomistic small angle scattering verification methods in[44] (this is in addition to the cases shown in Figure 5). This set includes monomer and multimer proteins both globular and elongated. We allow the parameters of the scattering model to vary for each structure but fix the geometric hydration layer as described above. The scattering

model is physically constrained in the same manner as in the FOXS[7] and Crysol[6] models, as discussed in detail in section 3 of the supplement. For the sake of brevity we also detail these results in section 3.6 of the supplement; it suffices to state here that the model performs comparably to the atomistic structure techniques and hence can be used to correctly infer protein structure from small angle scattering data.

Developing and testing and averaged scattering model for ab-initio prediction

In an ab-initio fitting it will be necessary to fix all parameters of the the scattering model so that the algorithm only alters the protein backbone parameters (the pairs (κ_i, τ_i)), this will allow the model to run in a reasonable time frame. In section 3.61 of the supplement we detail the construction of an averaged scattering model based on the set of parameters used for each successful fitting detailed in section 3.6 of the supplement. In general if this this average scattering model is then re-applied to the PDB structure and explicit hydration shell we do not obtain a sufficiently good fit to the scattering data (although it is not too far off).

The aim of this section is to show that we can use this averaged model and distort an initial PDB model in order obtain a high quality fit to the scattering data whilst still retaining a sufficiently realistic structure (within a few angstroms on average). This demonstrates ab-initio technique proposed here contains within its potential prediction population a high quality representation of the actual protein structure. It will also highlight some properties of the knot fingerprint statistic, by comparison to the widely used RMSD structural comparison statistic.

To perform this test we selected three pairs of proteins and crystal structure : Lysozyme (PDB:1LYZ), Ribonuclease (PDB:1C0B) and Bovine Serum Albumin (BSA, PDB:3V03, selecting a monomer unit) and scattering data obtained from the SAS database.[45] We used the PDB coordinates and secondary structure assignment as an initial input into the algorithm,

then we altered each secondary section individually using Monte Carlo sampling of the κ-τ distributions and the CB algorithm generate new structures. Using the hydration layer and scattering model, scattering curves were generated for these models. This process was run until a suitable fit to the scattering data was obtained.

Lysozyme and Ribonuclease

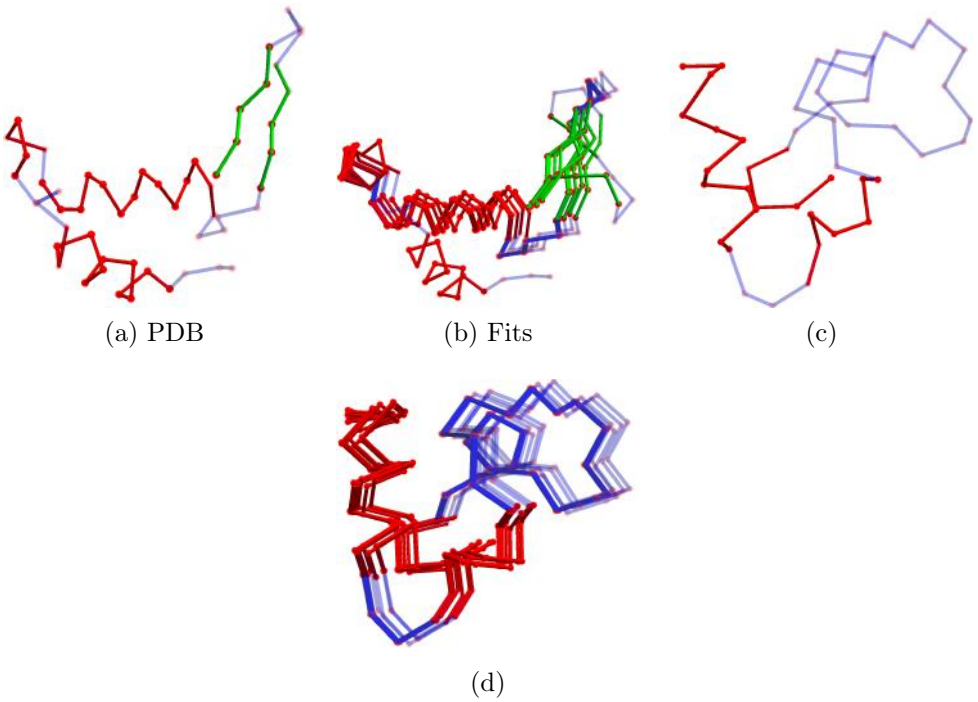

(a) PDB (b) Fits (c)

(d)

Figure 9: Sections of the 1LYZ PDB structure and example fits obtained by fitting our model to the scattering data. Panels (a) and (c) are subsections of the PDB, (a) has the sheet. Panels (b) and (d) are composite visualizations of the predictions.

Examples of the derived models obtained for Lysozyme are compared to subsections of the original PDB in Figure 9, we compare subsections for visual clarity. Typically the structures are nearly identical with only the occasional slight deviation in the geometry of some of the linker sections. This similarity is reflected in both the RMSD measures (calculated using the Biopython module[46]) and the knot finger print statistics, as shown in Figure 10(a). As one would expect both indicate excellent fits to the structure. There is a correlation of -0.3 between the two measures, a value on the edge of weak and reasonable. The results for

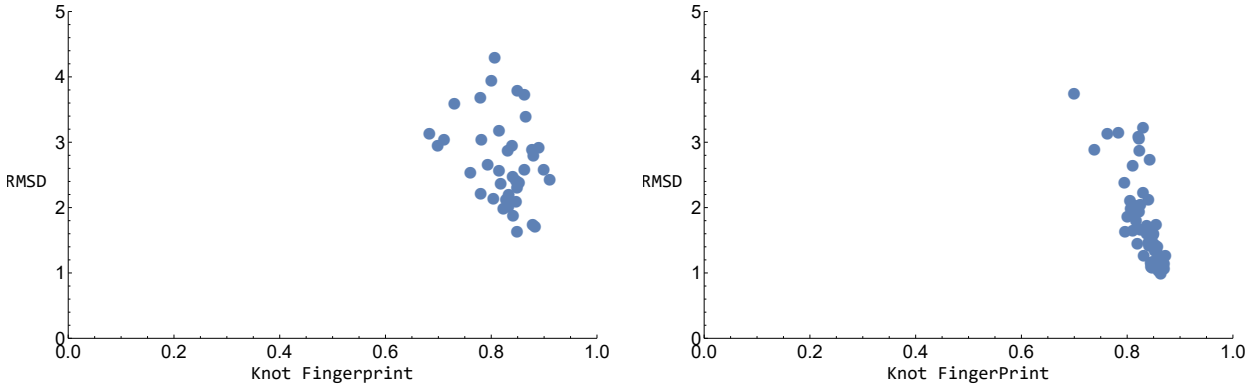

(a) (b)

Figure 10: A comparison of RMSD measures and Knot fingerprint statistics $\mathcal{K}_2$ for fittings of the model to scattering data for Lysozyme and Ribonuclease.These results are obtained using the PDB structure as the initial input to the algorithm and are by comparison to that PDB. (a) Lysozyme, (b) Ribonuclease.

Ribonuclease were very similar and the fit statistics are shown in Figure 10(b); again there is also a clear relationship between the knot fingerprint statistic and the RMSD measure, in this case the correlation is very strong, -0.8. We see this the correlation between the two measures as further justification of the knot statistic's appropriateness as a measure of structure.

BSA

Example fits to the (parts of the) larger BSA structure are shown in Figure 11, we only display sub-sections as the full molecule is too complex for a clear visual comparison, the sections where chosen at random and are indicative of the general comparison. Once again it is clear the structures are very similar.

So it is clear the model and method has the potential to correctly predict the tertiary structure of proteins accurately. From a purely ab-initio perspective the question now is how easy is it to get to the correct structure from a random initial guess? This question proves to be more complicated, requiring multiple predictions so for this preliminary study we focus on a single structure, Lysozyme.

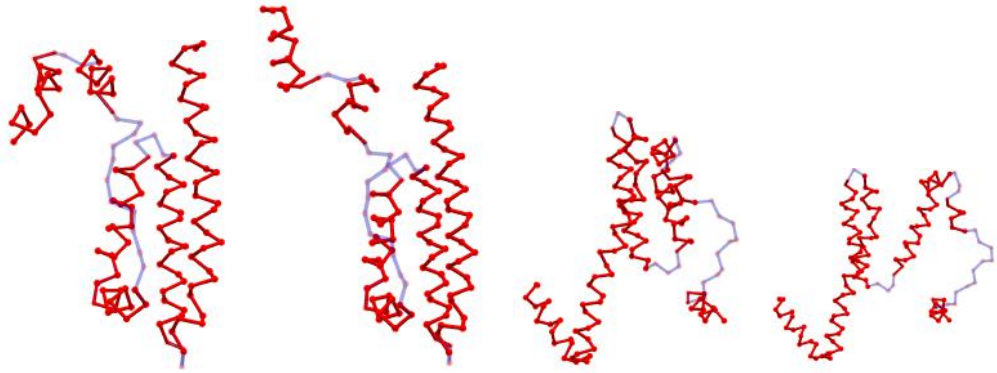

(a) PDB (b) Fit (c) PDB (d) Fit

Figure 11: Sections of the 3V03 PDB structure and example fits obtained by fitting our model to the scattering data. Panels (a) and (c) are subsections of the PDB. Panels (b) and (d) are example predictions.

Ab-initio prediction

In the case where no crystal structure is available, the secondary structure prediction based on the sequence alone can be used as a starting point. In order to test this ab-initio method we used the small angle scattering data of Lysozyme to make predictions of its structure. The process for obtaining a model is summarized in Figure 8. First an initial structure is randomly generated by the CB algorithm and surrounded with an explicit hydration layer (Figure 8(a)). A model scattering curve is calculated and compared to the experimental data (b). The curve is then changed by using a Monte-Carlo algorithm to generate new secondary structure units (along with a new hydration shell), thus altering the model's fold until it attains a sufficiently good fit to the scattering data Figure 8(c) and (d).

Once again we use the χ_f^2 statistic (11), but this time with additional constraint on the potential search space, contact predictions, based on a large number of homologous sequences. Data from the Raptor X web server[47] for the Lysozyme primary sequence were obtained. The C^α pairs with the 10 highest correlations were selected. An extra potential χ_{con} was added to the optimization statistic to ensure the distance between these pairs was restricted to be within 5 and 15 Å. If $l = 1, \ldots n_c$ labels the n_c pairs of constrained points

with mutual distances d_l^c then the quality of contact match χ_{con} is defined as follows:

$$\chi_{con} = \frac{C}{n_c} \sum_{l=1}^{n_c} \left(d_l^c - d_f^c \right)^2 , \tag{12}$$

with C a constant and d_c^f a reference distance (7 was used in this study). The value of C controls the likely variation in the distances d_c^l, a value of $C = 0.01$ in this study was found to give good results. In the following a model was considered a valid prediction when both $\chi_f^2 + \chi_{nl} + \chi_{con} < 0.008$ **and** $\chi_f < 0.008$ so that predictions had to simultaneously fit the scattering data and minimised the geometric penalties of not overlapping and also satisfying the contact predictions (to within a specified tolerance dictated by the constant C).

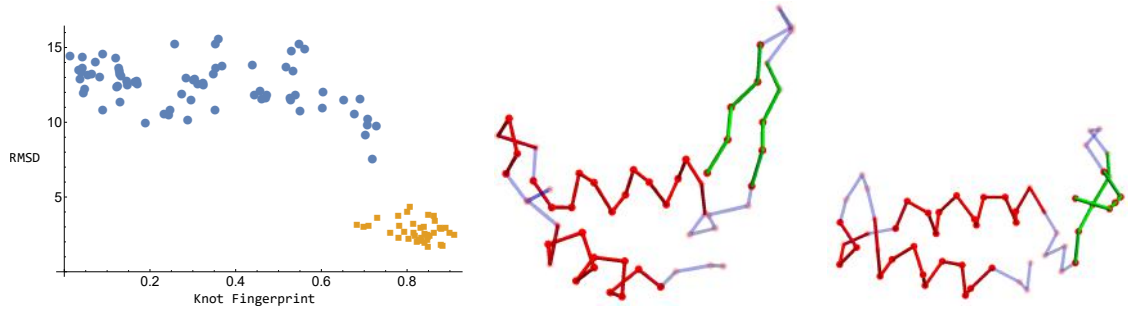

(a) (b) PDB Res 1:63 (c) Ab-initio fit Res 1:63

(d) PDB Res 64:129 (e) ab-initio fit Res 64:129

Figure 12: Ab-initio predictions for Lysozyme based on sequence data alone. Panel (a) depicts the RMSD and Knot statistic $\mathcal{K}_2(K_{pdb}, K_n)$ values for the predictions K_n, these are indicated as blue circles with the from-PDB data (Figure 10) shown as brown squares for comparison. Panel (b): secondary structure sections 1-10 (residues 1-63) of the 1LYZ crystal structure. Panel (c): secondary structure sections 1-10 of the best ab-initio fit. Panel (d): secondary structure sections 11- of the 1LYZ crystal structure (residues 64-129) . Panel (e): secondary structure sections 11- of the best ab-initio fit.

The results of the ab-initio fitting procedure are shown in Figure 12(a). The RMSD and knot fingerprint statistics, compared to the 1LYZ crystal structure are shown. The first

observation is that the best knot finger print statistics are comparable to the lower end of the from-PDB predictions obtained in the previous section. The second is that these correspond to the best RMSD measures. The apparent correlation between the two measures seems to remain for knot fingerprint statistics above 0.6. However, there is a gap between the best RMSD for the ab-initio predictions and those derived from the PDB structure. This is to be expected as the knot statistic is more tolerant of differences which preserve the entanglement (the general geometry of the fold). This difference can be seen visually in Figure 12 (b) and (c) which respectively represent the first 10 secondary structure sections of the 1LYZ crystal structure and the best fit ab-initio prediction (the one closest to the PDB predictions in Figure 12). The same fold-back of the two significant α-helical sections is present in both cases, as is the fold back of the β-sheet (although the variability in strand geometry allowed in the algorithm means they aren't identical). Further the relative orientation of this helical pair and the strand section is present is the same in both cases. So overall the basic fold geometry is correctly predicted which is why the knot statistic is so close to the PDB values. There are, however, a number of sections with some reasonably significant distance differences, for example the linker section joining the two helices; this means a bigger difference in the RMSD measure. Given all the difficulties associated with interpreting small angle scattering experiments we argue the knot statistic is a more appropriate measure of the accuracy of the prediction. One can see a similar conclusion can be applied to the rest of the molecule shown in Figure 12(d) and (e) for the PDB and fit respectively.

Objective prediction comparisons

Using only the protein sequence for secondary structure prediction and BioSAXS data we have been able to obtain tertiary structure models which can be observed and quantified to have a significantly similar fold geometry (topology) to the Lysozyme structure. However, a large number of predictions have knot statistics which suggest the structure's fold topology differs significantly from that of the crystal structure (Figure 12(a)). The target applications

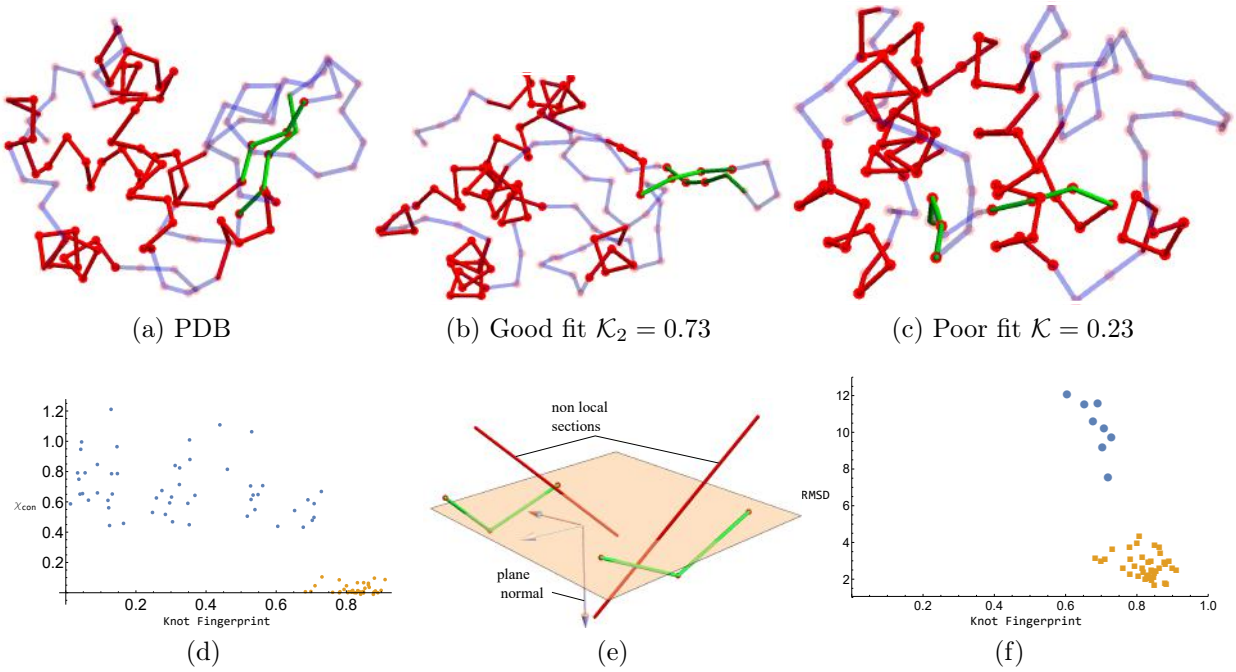

(a) PDB (b) Good fit $\mathcal{K}_2 = 0.73$ (c) Poor fit $\mathcal{K} = 0.23$

(d) (e) (f)

Figure 13: Comparisons of high $\mathcal{K}_2$ and low $\mathcal{K}_2$ Lysozyme predictions. Panel (a) is the PDB:1LYZ crystal structure. (b) A high quality fit ($\mathcal{K}_2 = 0.73$), (c) a low quality fit $\mathcal{K}_2 = 0.23$. (d) a comparison of the contact constraint χ_{con} and the knot finger print, the blue points (with larger values) are for the ab-intio fits and he brown dots are the from PDB fits. (e) two (green) sections of a sheet from Lysozyme model. A plane and its normal bisecting the strand sections is shown, also shown are two sections of the rest of the molecule which bisect the plane between the two strands. (f) the fingerprint-RMSD comparison plot with the screened ab-initio predictions.

for this method will be unknown structures and it must be established whether one could have identified these were “bad" predictions without the knowledge of the underlying structure.

To differentiate predictions we should seek objective structure comparison measures which do not depend on comparison known structural information (i.e. not to the PDB). One example would be the contact prediction statistic χ_{con}. This is objective in the sense that it only relies on sequence predictions, and would generally be available in target applications. A scatter plot of the knot statistic indicates the high quality ab-initio predictions (high $\mathcal{K}_2$) are less likely to have a high χ_{con} than the worse predictions, see Figure 13(d). If we were to run a significant number of predictions and then say select only those below the mean χ_{con} value then most of the high χ_{con} predictions remain, this could be a first means of filtering

the predictions, although we see it will still leave “bad" predictions so further analysis is required.

β sheet model variations and the power of knot statistics

Figure 13 shows the full 1LYZ crystal structure (a), a high $\mathcal{K}_2$ model (0.73) (b) with RMSD 9.21 (by comparison to the crystal structure) and a low $\mathcal{K}_2$ model (0.23) (c) with RMSD= 10.8. So there is a relatively small difference between the two prediction's RMSD measures, but a significant one as measure by the knot topological method. One clear difference is the isolation of the β-sheet. In both (a) and (b) the sheet is at one edge of the structure, whilst is (c) it is closer to the alpha helical secondary units of the structure, and further because its constituent strands of the prediction shown in (c) are not sufficiently closely related there appears to be a section of α-helix passing between them. This is a significant difference in entanglement detected by the knot based measure for (c) compared to (a) and (b). An inspection of the structures indicated that the better performing structures (in terms of their fingerprints) tended to have tighter and more isolated β-sheets, consistent with the examples illustrated. To try to quantify this we created two mathematical measures. The first measure is the mean distance between sequentially paired C^{α} atoms of the predicted sheet structure (this sequential dependence can be determined by distance measures and does not need a pre-determined knowledge of the strand orientation). We calculate this value for all predictions and choose those say less than the median value. The second is a discrete test as to whether any other section of the molecule passes “between the sheet". We approximate a plane for the sheet as indicated in Figure 13(e) and then determine if any other arcs of the main C^{α} chain pierce this plane, this this does occur we simply reject the structure as being physically unrealistic (as is the case in Figure 13(e)). Both are objective measures.

When the combination of sheet measures and the contact prediction cut-offs are applied we are left with a significant proportion of the high quality fits, including the one with the

lowest RMSD (Figure 13(d)). Crucially all the lower quality fits are filtered out. It should be noted that one of the high quality $\mathcal{K}_2 > 0.7$ predictions was lost during this filtering process, on the basis that its mean sheet distance was too high. This underlying selection mechanism should be generally applicable being based on basic principles, so there is an indication it will be possible to produce a general post-hoc selection procedure. In future it might be also be useful to use information such as sulphide bonding and hydrophobic exposure to further classify predictions.

Application to a novel protein with unknown 3D structure: the human SYCE1 core

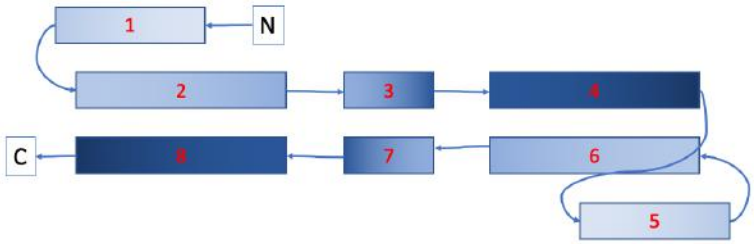

Figure 14: Schematic drawing of the SYCE1 construct with each box corresponding to one predicted alpha helix. The SYCE sequence of approximately 120 amino-acids corresponding to helices 1-4 is duplicated and linked by a tether to a repeat of the same sequence comprising of helices 5-8.

Based on the success of utilizing contact predictions to constrain potential models we applied the algorithm on the structural core of the human SYCE1 protein, a tethered construct where the sequence is repeated to allow formation of an extended anti-parallel coiled-coils with two short additional helices at each end that could fold back to form a small 3-helix bundle. The secondary structure of the tethered protein construct resulted in eight stretches of alpha-helices where based on the heptad repeats helices 2, 3, and 4, can be aligned to helices 6, 7, and 8 corresponding to the same sequence, respectively in an anti-parallel fashion. This resulted in 14 close contact predictions between helices 2 and 8, and helices 4 and 6, respectively, as shown in Figure 14.

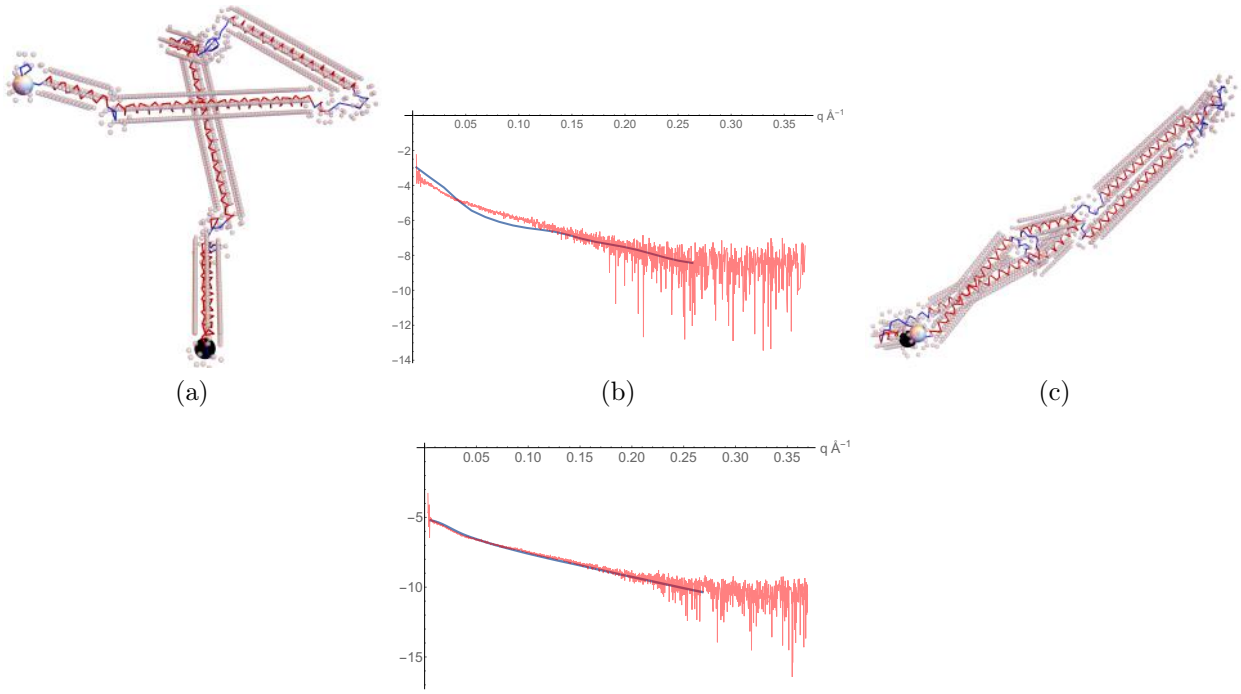

(a) (b) (c)

(d)

Figure 15: Illustrations of the optimization process used to obtain the model predictions forthe structural core of human SYCE1 . Panel (a) An initial configuration of the backbone based only on the sequence data shown in Figure 14. Also shown as spheres are the molecules of the hydration layer. Large black and white spheres indicate the end termini. (b) the scattering curve of the initial configuration (blue) over-layed on the scattering data (red). (c) the model prediction for which $\chi_f^2 + \chi_{nl} + \chi_{con} < 0.008$, the end termini are next to each other. (d) the final scattering curve compared to the experimental data.

Deriving the models

Based on the sequence and secondary structure predictions (a combination of those of Raptor X[47] and HHPRED[48]) 40 initial configurations were generated using the CB algorithm. An example is shown in Figure 15(a) along with its hydration layer, its scattering curve is compared to the experimental data (from[24]) in Figure 15(b). As shown the fitting is limited to the domain $q \in [0, 0.3]^{-1}$, which balances the twin consideration of a sufficient resolution and reliable signal to noise ratio. Using monte-carlo optimization the structure is altered until a reliable fit $\chi_f^2 + \chi_{nl} + \chi_{con} < 0.008$ is obtained, where the potential χ_{con} is based on the contact predictions described above. One such model is shown in Figure 15(c) along with its scattering curve in Figure 15(d). The identical chains of the structure have folded

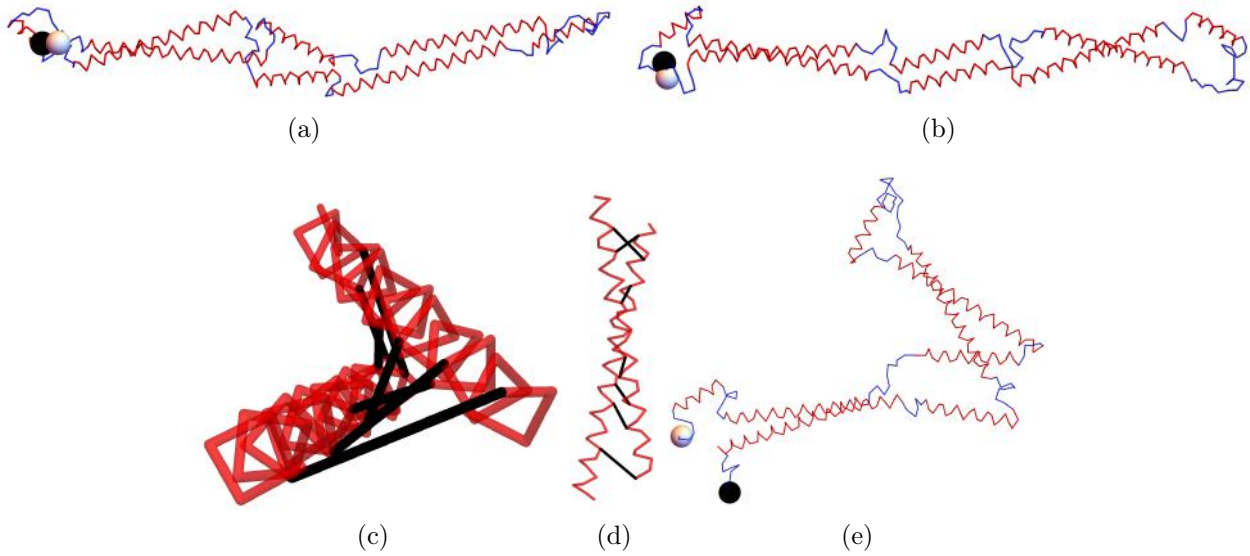

Figure 16: Illustrations of the model predictions. (a)-(b) are all model predictions. (c) One of the coiled coil units of (a) with black tubes representing the contact prediction distances, as see along the axis of the unit. (d) the tilted helical structure of the coiled coil unit. (e) a model obtained by minimising the chi-squared measure $\chi_{nl} + \chi_{con}$ only.

to lie (nearly) parallel with the end termini occupying a local neighbourhood. Two example models for which $\chi_f^2 + \chi_{nl} + \chi_{con} < 0.008$ are shown in Figure 16(a)-(b). Figures 16(c) and (d) indicate one of the coiled coil structures and depict the pairwise distances associated with the contact prediction terms χ_{con}. All models share the elongated bend shape with a anti-parallel coiled-coil arrangement of helix 2-4 to 6-8, respectively. The first helix in each helix (helices 1 and 5, respectively) show different orientations which reflect the expected conformational flexibility of the protein in solution. Importantly, the central coiled coil (made of helices 3 and 7, respectively) is not based on the constraints given a-priori but is entirely based on the optimization against the experimental data. Although a bead model results in a similar overall shape[24] our methods is able to derive a more detailed molecular model with distinct structural features such as the central coiled coil.

The experimental scattering data is crucial to the prediction quality

One might ask if the contact predictions alone were sufficient to predict the structure, since they are crucial to forming (some of) the coiled-coil structure. To test this we derived models by minimising the chi-squared measure $\chi_{nl} + \chi_{con}$ (*i.e.* ignoring the scattering data), a typical example is shown in Figure 16(e). The outer α-helicies are present as the contact prediction constraint χ_{con} force these structures to form. However, the whole structure is significantly folded. This folding was found to be a typical property of models obtained by minimsing only $\chi_{nl} + \chi_{con}$ and the degree of folding was far from consistent. The clear effect of further enforcing the model fit the scattering data is two-fold, first straightening out the whole structure and secondly, in doing so, developing a coiled-coil geometry in the middle of the structure.

Fitting to the scattering data and contact predictions is not straightforward

As a final note we note that of the 40 initial structures generated, only 5 obtained a suitably low combined chi -squared statistic ($\chi_f^2 + \chi_{nl} + \chi_{con} < 0.008$). All 5 structures, two of which are shown in Figure 16, were basically identical in this case (comparative $\mathcal{K}_2$ values > 0.9) so there was not need for any post-hoc structural comparison analysis. By comparison all 40 lead to models for which $\chi_{nl} + \chi_{con} < 0.008$. As we have just seen there is significant value in the extra information provided by the scattering data. The difficulty with obtaining suitable fits indicates that in the future more advanced optimization techniques than a straightforward monte-carlo search may be needed.

Discussion

This paper describes in depth the development of a tertiary structure model for BioSAXS data interpretation. A number of key points have been demonstrated with regards to its potential use to the structural biology community. Firstly, if the method takes as input

a structure with a similar tertiary structure to the target structure *e.g* a homology model or an incomplete (core) model for a structure, then it will likely find a highly accurate fit to the presumably correct structure, as verified on a benchmark set of proteins. Secondly, given a near complete absence of tertiary structural information, save that available from sequence data such as secondary structure predictions, the technique can generate realistic representations of the structure's fold. Further, in this ab-initio scenario there is the potential to reliably separate realistic predictions from those which are not biologically plausible, by both constraining the fitting procedure and applying optimization filtering. This final result, demonstrated here on Lysozyme is a significant result; there exists no purely ab-intio SAXS technique so far which has achieved such detailed predictions of the protein's fold (a number of techniques superimpose tertiary and secondary structure into ab-intio bead predictions but this requires extra information such as a valid homologous structure).

With regards to comparisons to existing techniques there are two categories to be discussed. The first is the set of different experimental methods used to derive structures in the protein data bank. The predictions from our methods, applied to small angle scattering data, can be near this level of quality **if** a reliable initial structural model is provided. This was demonstrated in the results section when we used PDB structures as a starting model, the algorithm yielded structures with RMSD measures (by comparison to the PDB structure) highly comparable to experimentally obtained models (for α carbon positions). In a purely ab-initio scenario our results indicate it is currently difficult to obtain this level of accuracy on a reliable basis (although one can get single angstrom RMSD measures). However, as shown in Figure 13(d), there is some indication that, if extra constraints such as contact predictions from homologous sequences can be enforced to a high degree of accuracy, there is the potential to reach similar levels of structural resolution to these alternative experimental techniques.

The second comparison would be to SAXS-specific ab-initio techniques for interpreting BioSAXS data. These include the bead based models such as GASBOR and DAMMIN/DAMMIF.[13,49]Howe

a direct comparison is not informative because as the nature of the prediction is different. Neither method makes explicit predictions of the tertiary structure of the molecule. Both are composed of effective scattering beads, the DAMMIN model aims to predict the volume occupied by the molecule by creating a cloud of beads whilst GASBOR does aim for a structure with a chain like nature constraining bead-bead distances, but there is no explicit secondary structure in the model. In the case of Lysozyme, can see that our predictions also have this property of occupying a similar volume to the crystal structure in Figure 13(a)-(c) thus is consistent with the low-resolution ab-intio bead teachniques (see *e.g.*[13]) . The advantage of our model is that it also makes an explicit prediction for the fold geometry of the secondary structure elements.

The ATSAS package does allow for the interpretation of bead models with tertiary structure through the use of the CORAL package.[49] Given known structures the package attempts to fit the structure into the bead model with a mixture of known (manually assigned) and unknown elements. This procedure was performed in[24] provide evidence that the SYC1E core modelled in section was a coiled-coil domain. Two coiled-coils were superimposed on a bead model with CORAL providing an additional linker section to join them. Our model simply uses the sequence data to determine the secondary structural elements, then it is able to try millions of differing (physically realistic) folds which and tests **each time** if they satisfy the scattering data, a much more direct and exhaustive test, which relies on far less user input. What is interesting is that this technique predicts an additional coiled-coil domain at the structure's centre, owing to the sequence interpretation splitting of the helical units. The method presented in this paper offers more flexibility in terms of using additional structural constraints and is more amenable to automated structural evaluation, with its main comparative advantage is the potentially exhaustive automated search of a space of potential tertiary folds with realistically constrained secondary structure.

Computation time

A single calculation comprising the CB algorithm, the generation of the hydration layer and calculation of the scattering curve takes of order 0.05 s for Lysozyme (128 residues) and 0.5 s for BSA (433 residues), both based on calculations performed on a single CPU, with the main cost coming from the Debye formula (5). As far as the actual optimization goes the timing can vary significantly, this depends on the number of secondary units which can be changed, the randomised initial condition and the difficulty in satisfying additional restrictions like the contact predictions (and how tightly they have been penalised). The ab-initio Lysozyme predictions generally varied between 10 min and an hour. For the SYCE1 chain (318 residues) it was closer to 20 hours (that said as mentioned above the predictions produced in this case were reliably accurate). In future we will look to implement Bayesian learning techniques for the search, as a large number of models suggested by the Monte-Carlo sampling overlap themselves and consistently trying such models wastes much time. This will be crucial to ensuring it can be run for larger molecules in future.

Number of initial models

One might ask how many predictions are required in order to obtain a viable structure (ab -intio). The examples here present a contrasting picture. The Lysozyme cases consistently produced structure which fit the scattering data, but as discussed only a relatively small percentage (about 8%) were considered a sufficiently good fit to the scattering data (*i.e.* a sufficiently low RMSD with respect to the PDB structure and high $\mathcal{K}_2$ value) and. By contrast from 40 initial conditions for the SYCE1 molecule only 12.5% were able to fit the scattering data, **but** all were near identical ($\mathcal{K}_2 > 0.9$) and excellent candidate structures. It is likely this is because Lysozyme is a globular protein whilst SYCE1 a very flat, linear structure. It is relatively easy to distort our model into a globular shape, but it allows for more structural variance, whilst the more linear structure is harder to form but much more constrained. The consistent evidence is that, currently, one might need at least 10

optimisation runs in order to obtain a good quality prediction. A future aim will be to better enforce contact predictions or other constraints during the fitting procedure in order to bring this ratio down.

Conclusion

As a solution-based technique, BioSAXS can provide structural information for targets where crystallisation and cryoEM techniques are challenging. In addition, the method allows data collection in a more natural environment than techniques such as crystallography and cryo-EM. Additionally, SAXS is not limited by protein size, as is the case for cryo-EM and NMR. Therefore, there is a clear need to develop the techniques for interpretation of this data in an ab-initio setting which improve on the levels of structural detail provided by the bead models currently popular.

In this paper we have shown that curve representation with hydration shell provides a molecular model for BioSAXS data with fits as good or better than traditional bead and envelope models. Unlike these models our model includes a complete secondary and tertiary model description. Importantly, starting from random models that only take secondary structure information and sequence-dependent distance constraints into account, a physically meaningful 3D model can be obtained by fitting models against the experimental data. That this is possible is due to the fact that the model is described with far fewer parameters compared to even a coarse-grain model that required three coordinates for each amino-acid **combined** with use of geometric constraints for regular secondary structural elements.

In order to show the potential of this ab-initio technique it was applied to a tethered core component of the human SYCE1 protein, for which no high-resolution structural data is available. The model derived was based on sequence information **alone** match those of a model that was previously reported in.[24] where the model was based on manual inspection of the sequences coupled with the fitting of ideal coiled coil segments to experimental scattering

data. Importantly, whilst the previously modelled structure includes two coiled coil segments, the model derived here recognised that this was the minimum number of segments required to explain the curved structure and that the true structure could consist of multiple coiled coils interrupted by short linkers. Thus, our novel ab-initio method has successfully generated a highly plausible model from experimental scattering data without the need for any more than minimal manual evaluation. This facility will be crucial for ab-initio structural determination (from biosaxs data) of larger molecules where it would not be practical to generate structures manually.

Further experimental information such as distance information from any other source can easily been added in the form of additional restraints into the optimization algorithm. The model's explicit description of realistic secondary structure means additional information, like contact predictions, radius of gyration, hydrophobicity of the chain and disulfide bonding can be employed as model constraints in the future. This will further enhance the accuracy of all potential models, and in particular help the end-user to distinguish mathematically correct but physically less likely models from correct solution. The secondary knot fingerprint statistic developed shows significant potential to evaluate structural similarity of models and hence to further automate this vital validation step.

The two future next steps are (i) the application of this method to multimeric structures where each known monomer structure can initially be treated as rigid-body and then refined in order to account for local changes in solution (ii) the application to larger, denovo structures where the exact 3D structure remains elusive. The second goal will require further refinements of the search space method of the optimization algorithm. The application to homo-multimers is straightforward and requires only minor addition to the existing code, we expect this to be the major initial application of our methods. Due to the limited information content of small-angle X-ray scattering data the ab-initio fold determination will depend on the accuracy of secondary structure prediction combined with appropriately weighted distance constraints such as those discussed above.

Acknowledgement

The authors would like to thank Christina Law for testing the scattering and hydration models. Financial support from the Biophysical Sciences Institute and the Addison-Wheeler fellowship for CP are gratefully acknowledged. We would also like to thank Dr Mark Miller whose knot identification code was used to calculate knot fingerprints as well as Prof Alain Goriely and Dr Andrew Hausrath for their input and advice in the development of the backbone model. Finally we are grateful to Dr Beth Bromley for her help with the contact predictions within the coiled coil of SYCE1.

Supporting Information Available

Additional deatails on the model's construction and testing are avaliable in the supplementary PDF [will be avaliable online in published version] This material is available free of charge via the Internet at `http://pubs.acs.org/`.

References

(1) Petoukhov, M. V.; Svergun, D. I. *The international journal of biochemistry & cell biology* **2013**, *45*, 429–437.

(2) Kikhney, A. G.; Svergun, D. I. *FEBS letters* **2015**, *589*, 2570–2577.

(3) Mina, J. G.; Thye, J. K.; Alqaisi, A. Q.; Bird, L. E.; Dods, R. H.; Grøftehauge, M. K.; Mosely, J. A.; Pratt, S.; Shams-Eldin, H.; Schwarz, R. T.; Pohl, E. *Journal of Biological Chemistry* **2017**, *292*, 12208–12219.

(4) Svergun, D. I.; Koch, M. H.; Timmins, P. A.; May, R. P. *Small angle X-ray and neutron scattering from solutions of biological macromolecules*; Oxford University Press, 2013; Vol. 19.

(5) Rambo, R. P.; Tainer, J. A. *Current opinion in structural biology* **2010**, *20*, 128–137.

(6) Svergun, D.; Barberato, C.; Koch, M. H. *Journal of applied crystallography* **1995**, *28*, 768–773.

(7) Schneidman-Duhovny, D.; Hammel, M.; Sali, A. *Nucleic acids research* **2010**, *38*, W540–W544.

(8) Poitevin, F.; Orland, H.; Doniach, S.; Koehl, P.; Delarue, M. *Nucleic acids research* **2011**, gkr430.

(9) Wright, D. W.; Perkins, S. J. *Journal of applied crystallography* **2015**, *48*, 953–961.

(10) Perkins, S. J.; et al, *Journal of applied crystallography* **2016**, *49*, 1861–1875.

(11) Schneidman-Duhovny, D.; Hammel, M.; Tainer, J. A.; Sali, A. *Nucleic acids research* **2016**, *44*, W424–W429.

(12) Franke, D.; Svergun, D. I. *Journal of applied crystallography* **2009**, *42*, 342–346.

(13) Svergun, D. I.; Petoukhov, M. V.; Koch, M. H. *Biophysical journal* **2001**, *80*, 2946–2953.

(14) Hausrath, A.; Goriely, A. *Journal of structural biology* **2007**, *158*, 267–281.

(15) Lundgren, M.; Krokhotin, A.; Niemi, A. J. *Physical Review E* **2013**, *88*, 042709.

(16) Kneller, G. R.; Hinsen, K. *Acta Crystallographica Section D: Biological Crystallography* **2015**, *71*, 1411–1422.

(17) Ramachandran, G. N.; Ramakrishnan, C.; Sasisekharan, V. *Journal of molecular biology* **1963**, *7*, 95–99.

(18) Bolcun-Filas, E.; Speed, R.; Taggart, M.; Grey, C.; de Massy, B.; Benavente, R.; Cooke, H. J. *PLoS genetics* **2009**, *5*, e1000393.

(19) Costa, Y. e. a. *Journal of cell science* **2005**, *118*, 2755–2762.

(20) Park, H. H. *Acta Crystallographica Section F: Structural Biology Communications* **2015**, *71*, 1131–1134.

(21) Davies, O. R.; Maman, J. D.; Pellegrini, L. *Open biology* **2012**, *2*, 120099.

(22) Syrjänen, J. L.; Pellegrini, L.; Davies, O. R. *Elife* **2014**, *3*, e02963.

(23) Dunce, J. M.; Dunne, O. M.; Ratcliff, M.; Millán, C.; Madgwick, S.; Usón, I.; Davies, O. R. *Nature structural & molecular biology* **2018**, 1.

(24) Dunne, O. M.; Davies, O. R. *Chromosoma* **2019**, 1–14.

(25) Carroll, D.; Hankins, E.; Kose, E.; Sterling, I. *The Mathematical Intelligencer* **2014**, *36*, 28–35.

(26) Majorek, K. A.; Porebski, P. J.; Dayal, A.; Zimmerman, M. D.; Jablonska, K.; Stewart, A. J.; Chruszcz, M.; Minor, W. *Molecular immunology* **2012**, *52*, 174–182.

(27) Wand, M. P.; Jones, M. C. *Kernel smoothing*; Crc Press, 1994.

(28) Putnam, C. D.; Hammel, M.; Hura, G. L.; Tainer, J. A. *Quarterly reviews of biophysics* **2007**, *40*, 191–285.

(29) Elias, M.; Wellner, A.; Goldin-Azulay, K.; Chabriere, E.; Vorholt, J. A.; Erb, T. J.; Tawfik, D. S. *Nature* **2012**, *491*, 134.

(30) Debye, P. *Annalen der Physik* **1915**, *351*, 809–823.

(31) Brown, P.; Fox, A.; Maslen, E.; O'Keefe, M.; Willis, B. *International Tables for Crystallography Volume C: Mathematical, physical and chemical tables*; Springer, 2006; pp 554–595.

(32) Kleywegt, G. J.; Jones, T. A. *Acta Crystallographica Section D: Biological Crystallography* **1998**, *54*, 1119–1131.

(33) Fraser, R.; MacRae, T.; Suzuki, E. *Journal of Applied Crystallography* **1978**, *11*, 693–694.

(34) Schwartz, R.; Istrail, S.; King, J. *Protein Science* **2001**, *10*, 1023–1031.

(35) Kufareva, I.; Abagyan, R. *Homology Modeling*; Springer, 2011; pp 231–257.

(36) Zemla, A.; Venclovas, Č.; Moult, J.; Fidelis, K. *Proteins: Structure, Function, and Bioinformatics* **2001**, *45*, 13–21.

(37) Millett, K. C.; Rawdon, E. J.; Stasiak, A.; Sułkowska, J. I. Identifying knots in proteins. 2013.

(38) Tubiana, L.; Orlandini, E.; Micheletti, C. *Progress of Theoretical Physics Supplement* **2011**, *191*, 192–204.

(39) Jamroz, M.; Niemyska, W.; Rawdon, E. J.; Stasiak, A.; Millett, K. C.; Sułkowski, P.; Sulkowska, J. I. *Nucleic acids research* **2014**, *43*, D306–D314.

(40) Sułkowska, J. I.; Rawdon, E. J.; Millett, K. C.; Onuchic, J. N.; Stasiak, A. *Proceedings of the National Academy of Sciences* **2012**, *109*, E1715–E1723.

(41) Diamond, R. *Journal of molecular biology* **1974**, *82*, 371–391.

(42) Rolfsen, D. *Knots and links*; American Mathematical Soc., 2003; Vol. 346.

(43) Rambo, R. P.; Tainer, J. A. *Nature* **2013**, *496*, 477.

(44) Schneidman-Duhovny, D.; Hammel, M.; Tainer, J. A.; Sali, A. *Biophysical journal* **2013**, *105*, 962–974.

(45) Valentini, E.; Kikhney, A. G.; Previtali, G.; Jeffries, C. M.; Svergun, D. I. *Nucleic acids research* **2014**, *43*, D357–D363.

(46) et al, C. *Bioinformatics* **2009**, *25*, 1422–1423.

(47) Peng, J.; Xu, J. *Proteins: Structure, Function, and Bioinformatics* **2011**, *79*, 161–171.

(48) Zimmermann, L.; Stephens, A.; Nam, S.-Z.; Rau, D.; Kübler, J.; Lozajic, M.; Gabler, F.; Söding, J.; Lupas, A. N.; Alva, V. *Journal of molecular biology* **2018**, *430*, 2237–2243.

(49) Petoukhov, M. V.; Franke, D.; Shkumatov, A. V.; Tria, G.; Kikhney, A. G.; Gajda, M.; Gorba, C.; Mertens, H. D.; Konarev, P. V.; Svergun, D. I. *Journal of applied crystallography* **2012**, *45*, 342–350.